CHAPTER 17

Spectral characteristics of resting state networks

Rami K. Niazy[†], Jingyi Xie[‡], Karla Miller[‡], Christian F. Beckmann[‡] and
Stephen M. Smith[‡,*]

[†] *Biomedical Physics Department, King Faisal Specialist Hospital & Research Centre, Riyadh, Saudi Arabia*
[‡] *Centre for Functional Magnetic Resonance Imaging of the Brain (FMRIB), University of Oxford, Oxford, UK*

Abstract: Resting state networks (RSNs), as imaged by functional MRI, are distributed maps of areas believed to be involved in the function of the "resting" brain, which appear in both resting and task data. The current dominant view is that such networks are associated with slow (~ 0.015 Hz), spontaneous fluctuations in the BOLD signal. To date, limited work has investigated the frequency characteristics of RSNs; here we investigate a range of issues relating to their spectral and phase characteristics. Our results indicate that RSNs, although dominated by low frequencies in the raw BOLD signal, are in fact broadband processes that show temporal coherences across a wide frequency spectrum. In addition, we show that RSNs exhibit different levels of phase synchrony at different frequencies. These findings challenge the notion that FMRI resting signals are simple "low frequency" spontaneous signal fluctuations.

Keywords: functional MRI; resting state networks; RSN; default mode; empirical mode decomposition; Hilbert–Huang transform; independent component analysis.

Introduction

Resting state networks (RSNs) in functional magnetic resonance imaging (FMRI) are distributed maps of brain areas, which are believed to be involved in the function of the "resting" brain and which appear in both resting and task data. Previous studies have described RSNs as low-frequency (~ 0.015 Hz), spontaneous oscillations in the BOLD response during resting state (Biswal et al., 1995). Studies that have used these observations to study functional connectivity between brain areas have generally concluded that these signals are of neuronal origin (Biswal et al., 1995; Lowe et al., 1998; Xiong et al., 1999). Biswal et al. (1995) were the first to demonstrate the use of RSNs to detect functional networks in the primary motor cortex during rest. The specific areas were identified by performing a

*Corresponding author.
Tel: +44 (0) 1865 222726; Fax: +44 (0) 1865 222717
E-mail: steve@fmrib.ox.ac.uk

correlation analysis between the resting time series of a seed voxel in the primary motor cortex (initially identified from FMRI under a motor task) and all other voxels in the brain. The time-course of the seed voxel was found to be uniquely and significantly correlated with other sensorimotor cortex locations. The frequency spectrum of these voxels peaked at around 0.02 Hz. Similar results were obtained by Lowe et al. (1998) and Xiong et al. (1999) using different TRs, slice prescriptions, and different seed voxels within the motor cortex. More recent studies have shown that connectivity in resting data is affected by aging (Damoiseaux et al., 2008; Lai et al., 2002; Niazy et al., 2002) and pathological processes such as multiple sclerosis (De Luca et al., 2002) and Alzheimer's disease (Greicius et al., 2004; Rombouts et al., 2009). Beckmann et al. (2005) provided evidence that RSNs are not simply a result of physiological noise, such as the cardiac cycle or respiration. RSNs have also been shown to be a consistent and reproducible phenomenon across subjects and reside in the gray matter (Beckmann et al., 2005; Damoiseaux et al., 2006; De Luca et al., 2006). Of particular interest in RSNs is a unique network dubbed the default mode network (DMN), which has been suggested to be a network whose job is to maintain the brain in an idle and "ready" or "default" mode (Raichle et al., 2001). Other studies have attributed BOLD fluctuations in the DMN to neuronal activities involved in "mind wandering" (Mason et al., 2007) and sleep (Fukunaga et al., 2006).

The temporal characteristics of RSNs have received little attention aside from the occasional spectral analysis showing the peaks at low frequency. Cordes et al. (2001) have studied the contribution of different frequencies to functionally connected areas during rest. They found that frequencies <0.1 Hz accounted for 90% of the cross correlation values between the connected areas. This range, however, is still very large and close to the Nyquist frequency of most FMRI studies (with typical TR of 3 s). In addition, the analysis in that study does not address the question of how the different frequencies are related,

that is, ask whether the different frequencies are part of the same process or not. More recently, Chang and Glover (2010) investigated temporally varying characteristics of RSNs, including the use of wavelet decomposition to study coherence between different RSNs as a function of frequency and time, coming to the general conclusion that correlation/coherence between different networks changes over time.

Currently, within the neuroimaging community, the term "resting state networks" is used almost synonymously with "low-frequency fluctuations." Although previous research in this area has shown the dominance of low frequencies, to date no one has explicitly attempted to isolate underlying processes in order to comprehensively describe the temporal characteristics. Solely looking at RSNs' frequency spectra may be overly simplistic; this is largely due to the inherent assumptions of linearity and stationarity in a Fourier analysis, two assumptions which have not been validated in the context of RSNs.

In this chapter, we explore the frequency and phase characteristics of RSNs. The first section explores FMRI RSNs across the frequency spectrum as well as characterizing the relationship between the different frequencies and RSNs. In the second section, we further demonstrate the broadband characteristics of RSNs using hemodynamic deconvolution to estimate the frequency spectra of the underlying "neuronal" processes, concentrating on the highest estimable frequencies. Finally, the third section bolsters the broadband argument from perfusion RSN data, concentrating on the lowest frequencies.

FMRI RSNs across the frequency spectrum

Independent component analysis

Independent component analysis (ICA; Bell and Sejnowski, 1995; Comon, 1994; McKeown et al., 1998) is a technique which decomposes a two-dimensional matrix (e.g., time × voxels) into a

set of time-courses and associated spatial maps. These jointly describe the temporal and spatial characteristics of underlying mixed signals (components). A probabilistic independent component analysis (PICA; Beckmann and Smith, 2004) model extends this by assuming that the p-dimensional vectors of observations (time series in the case of FMRI data) are generated from a set of q ($<p$) statistically independent non-Gaussian sources (spatial maps) via a linear and instantaneous "mixing" process corrupted by additive Gaussian noise. In this work, PICA was applied to FMRI data acquired under rest in order to identify RSNs' spatial maps and associated time-courses. The Hilbert–Huang transfrom (HHT) was then applied to the time-courses associated with the RSN spatial maps provided by PICA in order to analyze their temporal characteristics as described below. For more information about PICA, see Beckmann and Smith (2004).

The HHT and empirical mode decomposition

The HHT (Huang et al., 1998, 1999) consists of two parts: the empirical mode decomposition (EMD) and the Hilbert spectral analysis (HSA). EMD is the algorithm by which a single time-course is decomposed into its oscillatory components. HSA is then applied to calculate the instantaneous phase and frequency of the resulting components—the result of which can then be displayed in the time-frequency space. In this work, we are only interested in EMD and the subsequent calculation of phase, and thus only these parts will be explained here. For a thorough introduction to HHT and its application, see Huang and Shen (2005).

EMD is a data driven, adaptive algorithm that decomposes any time series into its intrinsic modes of oscillation, subsequently allowing the calculation of the instantaneous phase and frequency from these components. In EMD, the only assumption made is that the signal of interest consists of added amplitude- and frequency-modulated (AM and FM) oscillatory components of different frequencies regardless of the linearity or the stationarity of the underlying generating processes. Each oscillatory component is called an *intrinsic mode function* (IMF). The definition of an IMF is a function that meets the following two conditions:

1. The number of zero-crossings and extrema, in the whole of the dataset, are the same or differ at most by 1.
2. At any point in the function, the local mean, defined as the mean of the upper and lower envelopes, is zero.

The EMD algorithm is a heuristic but intuitive process for finding IMFs: since any deviation from the local mean is a result of overriding waves, iteratively removing this mean until a zero-mean is achieved yields an IMF. Figure 1 shows a schematic flowchart of the EMD algorithm.

For a signal $\mathbf{X}$, we set $\mathbf{S} = \mathbf{X}$ and then find the local maxima and minima in the signal $\mathbf{S}$. The upper envelope, $\mathbf{E}_{max}$, of the signal is then found using cubic spline interpolation of the maxima points. Similarly, the lower envelope, $\mathbf{E}_{min}$, is calculated using the minima points. An IMF candidate, $\mathbf{H}_1$, can then be calculated by subtracting the resulting mean of the envelopes, $M_1 = (\mathbf{E}_{max} + \mathbf{E}_{min})/2$, from the data:

$$H_1 = S - M_1. \qquad (1)$$

Ideally, $\mathbf{H}_1$ would be an IMF. In practice, however, the first candidate does not usually meet the IMF conditions. In that case, $\mathbf{S}$ is set to $\mathbf{H}_1$ and the envelopes are found and their mean is subtracted iteratively until the first IMF is found. This process is referred to as the *sifting* process. When the first IMF component, $\mathbf{C}_1$, is found after k siftings, it can be written as

$$C_1 = H_k = S - M_k, \qquad (2)$$

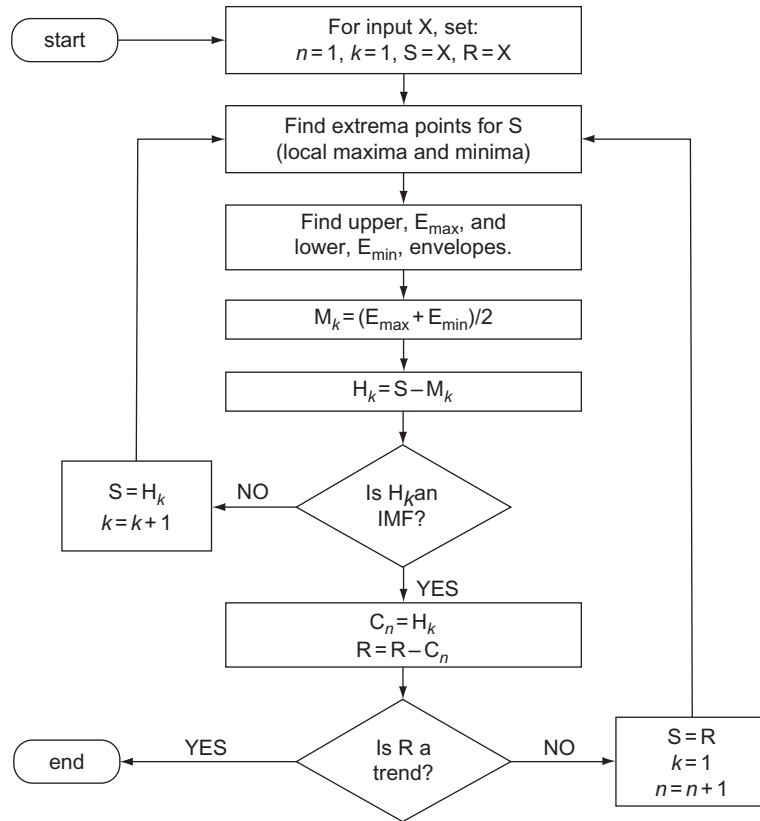where $\mathbf{S} = \mathbf{H}_{k-1}$, and the residue after the first IMF is the data minus $\mathbf{C}_1$:

262

Fig. 1. EMD algorithm flowchart. To initialize, **S** and **R** are set to be the input signal **X**. **S** is the signal on which the sifting is performed, and **R** is the residue. To start, the upper, $\mathbf{E}_{max}$, and lower, $\mathbf{E}_{min}$, envelopes are calculated for **S**. The mean of the envelopes, **M**, is subtracted from **S** to produce an IMF candidate, **H**. This constitutes one sifting iteration. If **H** does not meet the IMF definition, **S** becomes **H** and the sifting continues on **S** and a new candidate, **H**, is found. This is repeated until a candidate is found that meets the IMF definition. This candidate becomes an IMF component, **C**. The IMF is then subtracted from the residue and a new residue, **R**, is calculated. If **R** is not a monotonic trend, **S** is set to the new residue and the process is repeated until all IMFs are found and the residue becomes a monotonic trend. The subscripts k and n are used to index the sifting iteration number (per IMF) and the number of IMFs, respectively.

$$R_1 = X - C_1 \tag{3}$$

or more generally

$$R_n = R_{n-1} - C_n, \ \forall n > 1. \tag{4}$$

The first IMF is the component with the highest frequency content or shortest timescale. If the residue is not a trend, that is, does not have more than 1 extrema point, **S** is set to **R** and another round of siftings is performed to find the next IMF. This is repeated until all IMFs are found and the residue becomes a monotonic trend. Figure 2 shows a complete example decomposition using an FMRI signal. After the EMD is complete, the original signal can be written in terms of the IMFs as
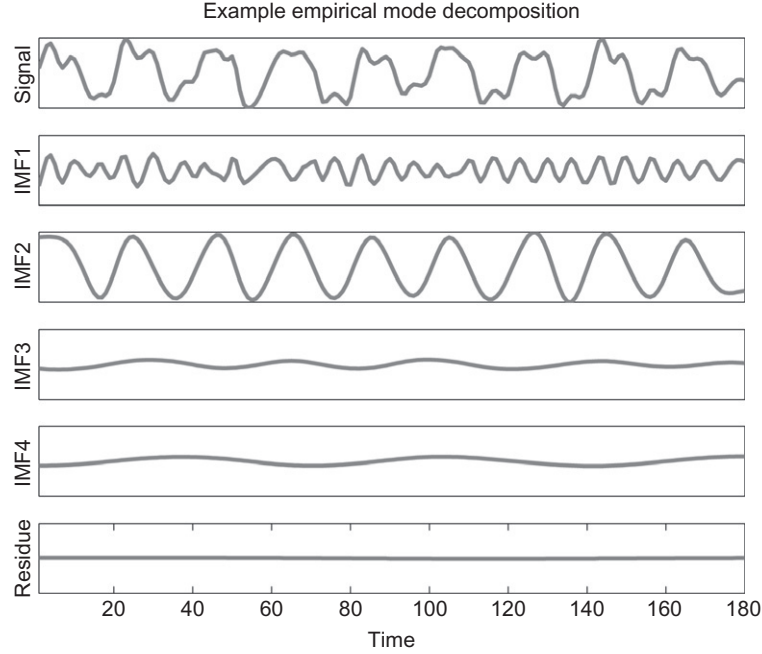
Example empirical mode decomposition

Fig. 2. Full EMD on an example signal. The signal is an FMRI signal from an activated voxel in a block-design experiment.

$$X = \sum_{n=1}^{N} C_n + R_N, \qquad (5)$$

where N is the number of IMFs found and $\mathbf{R}_N$ is the residue after the Nth IMF.

A critical decision in the EMD algorithm is the stopping criteria for the sifting process, as over-sifting yields constant amplitude FM components (Huang et al., 1998). The discussion of the ideal stopping criteria is beyond the scope of this work and the reader is referred to the literature for a more in-depth discussion of this issue (Huang et al., 1998, 1999; Rilling et al., 2003). For our data, we used the stopping criteria suggested by Huang et al. (2003): the sifting was stopped when the number of extrema and zero-crossings was constant for four consecutive sifting iterations.

The instantaneous phase and frequency of the IMFs can now be calculated using the Hilbert transform. For a signal $x(t)$, the Hilbert transform is defined as

$$\mathcal{H}[x(t)] = y(t) = \frac{1}{\pi} P \int_{-\infty}^{\infty} \frac{x(\mathcal{T})}{t - \mathcal{T}} d\mathcal{T}, \qquad (6)$$

where P is the Cauchy principal value. The signals $x(t)$ and $y(t)$ form a complex conjugate pair for which the analytic signal, $z(t)$, of $x(t)$ can be written as

$$z(t) = x(t) + iy(t) = a(t)e^{i\theta}(t) \qquad (7)$$

and the instantaneous amplitude, phase, and frequency can be calculated as

$$a(t) = \sqrt{x^2(t) + y^2(t)}, \qquad (8)$$

$$\theta(t) = \arctan\left(\frac{y(t)}{x(t)}\right) \qquad (9)$$

and

$$\omega(t) = \frac{d\theta(t)}{dt}. \qquad (10)$$

Although convenient, the values obtained from Eqs. (6) to (10) are not very useful when applied to raw real-world signals. As can be seen in Eq. (10), the result is a single value at any given time, which means that the signal needs to be a "monocomponent" or narrow-band signal, with one defined frequency at any given time point, for the results to make sense or have a physical meaning. Band-passing a signal to achieve a narrow-band signal is counterproductive given the desired outcome of adaptively characterizing a signal. In addition, any shift in the mean of the signal (non-zero-mean) also yields meaningless instantaneous frequency values. Ideally, one needs to disentangle the different oscillatory components and trends that make up the signal without distorting them, that is, preserving their nonlinear features. We can achieve this using the EMD algorithm. Then, we can apply Eqs. (6)–(10) to any IMF to give meaningful results.

Investigating FMRI RSNs

Six subjects participated in this study (healthy, aged 20–40 years). One session per subject of FMRI scanning was performed using a Varian INOVA 3-Tesla MRI system. A head-only gradient coil was used, with a birdcage head coil for pulse transmission and signal reception. A whole-brain, gradient echo-planar imaging (EPI) sequence was used with the following parameters: TR = 3 s; TE = 30 ms; FOV = 190 mm with 64×64 imaging matrix (3×3 mm in-plane resolution); 600 volumes; 46 3 mm axial slices. The FMRI scan was performed during 30 min of behavioral rest. Subjects were instructed to keep their eyes open, fixate their gaze, and stay alert throughout the scan.

PICA was performed on all datasets using MELODIC (Beckmann and Smith, 2004), part of FSL. A fixed dimensionality reduction for all decompositions was used with 40 independent components obtained per dataset. Four consistent (across subjects) RSNs were identified manually from each ICA decomposition for further analysis. The four selected RSNs were chosen for their consistency and to match some of the principal RSNs identified originally by Beckmann et al. (2005) and later validated against a task-activation meta-analysis database as also corresponding to task coactivation networks by Smith et al. (2009). The four investigated RSNs are shown in the first column of Fig. 3 from a representative subject. Following the identification convention used by Beckmann et al. (2005), the four RSNs were the DMN, the medial visual cortical area, the auditory/sensory cortex, and the motor/spatial attention cortical areas. These are rough descriptions from the dominating functional areas in each RSN. Henceforth, we will refer to these as RSN1–RSN4.

In order to attempt to isolate possible underlying oscillatory processes within each of the RSNs, we performed a separate EMD on each RSN's time-course. This process creates a set of IMFs which represent underlying simple fluctuations and which jointly explain the overall estimated time-course, while also each being a sparse representation (of one aspect of the data) in the time–frequency domains. Importantly, unlike a simple Fourier analysis, these oscillations are generated without assuming stationarity and linearity.

In order to assess the spatial specificity of these oscillations, we used the resulting IMFs as regressors in GLM analysis to identify if any one of the underlying simple oscillations primarily contributes to the spatial structure of the RSN. Given that the IMFs are almost orthogonal, the analysis can be done by using all the resulting IMFs from one RSN as the explanatory variables (EVs) in the design matrix of the GLM analysis. Therefore, one GLM analysis was performed per RSN per subject.

The FMRI results showed that at least the top four IMFs of each RSN (the first four IMFs starting with the highest frequency) correlated significantly with the RSN they were derived from, in all subjects.
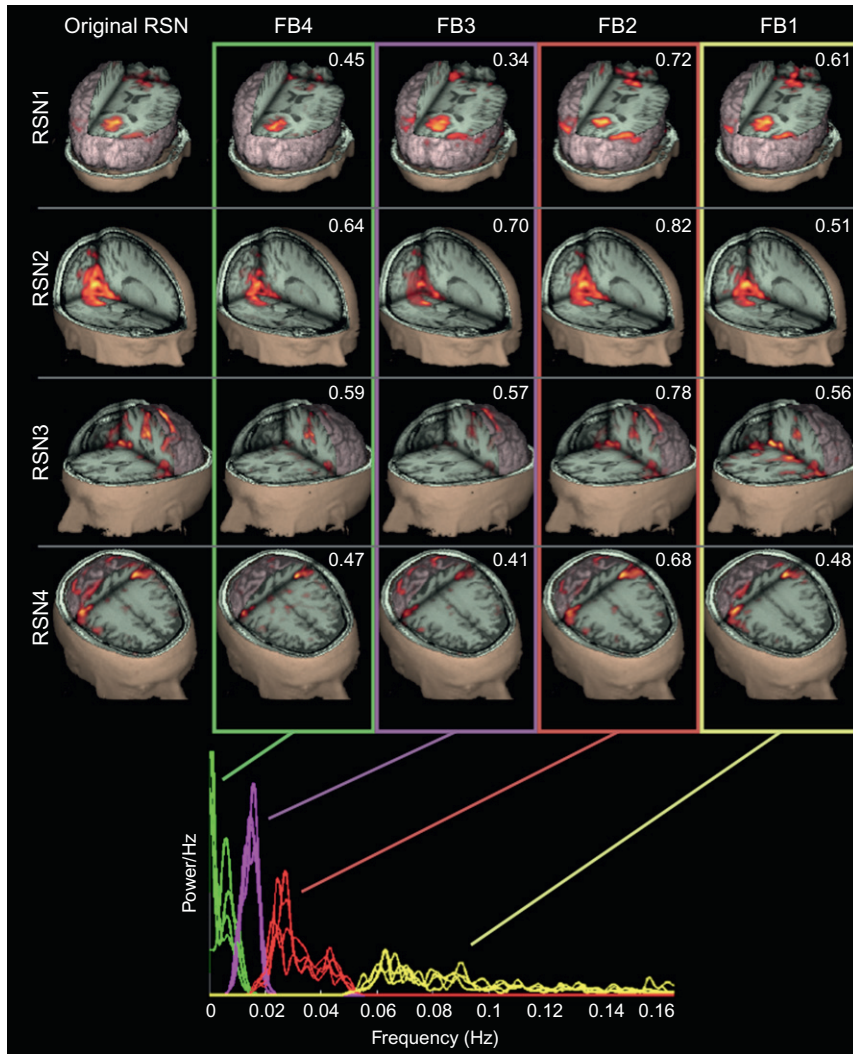
Fig. 3. RSNs from a representative subject. The first column shows the original RSNs obtained using PICA. Columns two to five show the RSNs obtained in the filtered data using FB4, FB3, FB2, and FB1, respectively. The frequency spectra of the filtered data RSNs are shown in the bottom of the figure, color-coded according to the frequency band. The value shown on the top-right corner of each image is the dice similarity coefficient (DSC) between that RSN and the original RSN from the unfiltered data.

The re-regression inherent to the method outlined above may seem circular (though it is not—see the discussion section), and further analysis was performed to validate the results: First, the reader is reminded that each IMF of any given RSN occupies a unique frequency band—the first IMF occupies the highest frequencies, the last occupies the lowest—some slight overlap is present. Further, as the frequency content of the different RSNs (and subjects) are roughly similar, the same IMF number from any number of RSNs will roughly occupy the same frequency

band. Hence, it is possible to validate the obtained results by band-pass filtering the FMRI data using a bank of filters with pass-band characteristics similar to those occupied by the top four IMFs, then rerunning PICA to test whether the RSNs still exist. Based on the frequency characteristics of the four dominant IMFs, the FMRI data of each subject were filtered using four band-pass filters with the following frequency band-pass characteristics: 0.004–0.01, 0.01–0.02, 0.02–0.05, and 0.06–0.15 Hz, resulting in a total of five datasets per subject (original data plus the four band-pass filtered versions). For consistency with the correspondence between the frequency content and the number of the IMF, that is, lower number has highest frequency content, the four mentioned filters will be referred to, respectively, as FB4, FB3, FB2, and FB1 (again, with the highest frequency content in FB1 and the lowest in FB4). PICA was run again on the filtered datasets and the results checked for the presence of RSNs.

In addition, within-subject phase synchrony between IMFs (top four) of the same RSN, and between the same IMF from the different RSNs, was evaluated. This was done by first calculating the phase function for each of the top four IMFs using Eqs. (6)–(10). Once the phase functions were calculated, phase synchrony between any number of N phases, θ_n, $n = 1, 2, 3, \ldots, N$, can be calculated as

$$\rho = \left[\left(\frac{1}{N} \sum_{n=1}^{N} \sin\theta_n \right)^2 + \left(\frac{1}{N} \sum_{n=1}^{N} \cos\theta_n \right)^2 \right]^{\frac{1}{2}},$$
$$0 \leq \rho \leq 1$$

(11)

When Eq. (11) is applied in our case, the result is a phase synchrony function, $\rho(t)$, as the equation is applied one time point at a time, across the phases of the different IMFs of interest. Equation (11) is referred to as *intertrial phase coherence* by Delorme and Makeig (2004), where it is used to quantify the phase coherence between

event-related potential (ERP) trials in any specified frequency.

Statistical significance of the level of phase synchrony was established using permutation testing. In the case of phase synchrony between the same IMF across the different RSNs, a distribution was built by randomly selecting the IMF of interest from one of the six subjects for all RSNs, then measuring the mean phase synchrony and repeating the procedure many times until a distribution is built. For example, in testing for IMF1 phase synchrony across the four RSNs, one of the six IMF1s available (from the six subjects) for RSN1 is selected at random from the group. A similar random selection is done from the six IMF1s of RSNs 2, 3, and 4. A phase synchrony time-course is then calculated from the four selected IMF1s, and the mean of the time-course becomes one point in the probability density function (PDF). The operation is performed 1000 times to build the whole PDF for the synchrony of IMF1. The mean phase synchrony for IMF1 for every subject is then checked for significance against the PDF at the desired threshold. The same is done for IMFs 2, 3, and 4. The same approach was used for testing the significance of phase synchrony across the different IMFs of a given RSN. Taking RSN1 as an example, here, first an IMF1 is selected at random from the six available for RSN1. Then, similarly, random IMFs 2, 3, and 4 are selected from the six available per IMF. The phase synchrony here is measured across the four IMFs of RSN1 and the mean of the phase synchrony time-course becomes an entrant in the PDF. The process is repeated 1000 times until a PDF for RSN1 is built. Similarly, PDFs for RSNs 2, 3, and 4 are built against which phase synchrony from each subject can be compared for significance. A $p < 0.05$ value for all tests was used.

The results of the GLM analysis showed FMRI maps correlated with each of the top four IMFs, reproducing the original RSN as obtained using PICA (results not shown). Similar results were obtained from all subjects. These initial results

are somewhat surprising as they indicated that the RSNs are not just "low-frequency fluctuations" in the BOLD signal. However, as some concerns could be voiced as to whether the approach of using the IMFs obtained from the RSN time-courses was circular in nature (see Discussion section), a validation approach using filtering was used as described earlier.

Figure 3 shows RSNs obtained using PICA on the filtered data of a representative subject. The dice similarity coefficient (DSC) between each RSN reproduced from the filtered data and the original RSN is shown in the top-right of each image. Although all RSNs were reproducible across the four frequency bands, RSNs 1 and 2 (the highest frequencies) were the most reproducible. The first column, labeled Original RSN, is the original RSN obtained from running PICA on the original FMRI data. Columns 2–5 show the RSNs from running PICA on the data filtered using FB4, FB3, FB2, and FB1, respectively. As can be clearly seen, the DSC values were high for all RSNs. Table 1 shows the mean DSC values across the six subjects along with the standard deviation. All subjects showed similarly high DSC values. Note that the highest DSC values were consistently obtained in FB2, and not in FB3, where the oft-reported RSN frequency (~0.015 Hz) lies.

Figure 4a shows the results of testing the significance of phase synchrony between the IMFs of any given RSN. The results from the six subjects are plotted against the null distributions (represented as box plots) along with the significance threshold. The mean phase synchrony calculations from almost all subjects were significant ($p < 0.05$).

Figure 4b shows the results from measuring the phase synchrony of any given IMF across the four RSNs, in any given subject. This is a measure of how any given frequency (IMF number) is synchronous across all four RSNs compared to the null distribution. Again, the results from the six subjects are plotted in red. One particular subject of the six was always the least significant in all the IMFs. Qualitatively, at least for IMFs 2 and 3, all subjects were clustered around the significance threshold. IMF 3 was the most consistent in showing significant synchrony, which includes the frequency of 0.015 Hz, the traditional "low-frequency fluctuation" frequency of RSNs.

Finally, Fig. 5 shows the RSN power spectra of each subject individually. This figure reveals that although any given RSN does not seem to share distinguishing spectral properties across subjects, the different RSNs in any given subject have quite similar spectra.

In the next section, we take a further look at the power spectra of RSNs, particularly with respect to their characteristics toward the higher frequency range.

RSN spectra after correcting for the effects of HRF blurring

RSNs as observed with FMRI have been widely described as being "low frequency," because spectral analysis shows the strongest fluctuations at the lowest frequencies. Some refer to this as

Table 1. Mean dice similarity coefficient (DSC) values across subjects

	FB4	FB3	FB2	FB1
RSN1	0.5001($\pm$0.12)	0.5270($\pm$0.15)	0.6084($\pm$0.18)	0.5155($\pm$0.12)
RSN2	0.5088($\pm$0.09)	0.4961($\pm$0.16)	0.7311($\pm$0.11)	0.5203($\pm$0.09)
RSN3	0.4656($\pm$0.12)	0.4778($\pm$0.16)	0.5665($\pm$0.19)	0.4630($\pm$0.15)
RSN4	0.3914($\pm$0.08)	0.4441 ($\pm$0.09)	0.4728($\pm$0.13)	0.4498($\pm$0.12)

Each entry in the table is the average DSC values across subjects calculated between the original RSN (row) and the reproduced RSN in the corresponding frequency band (column).
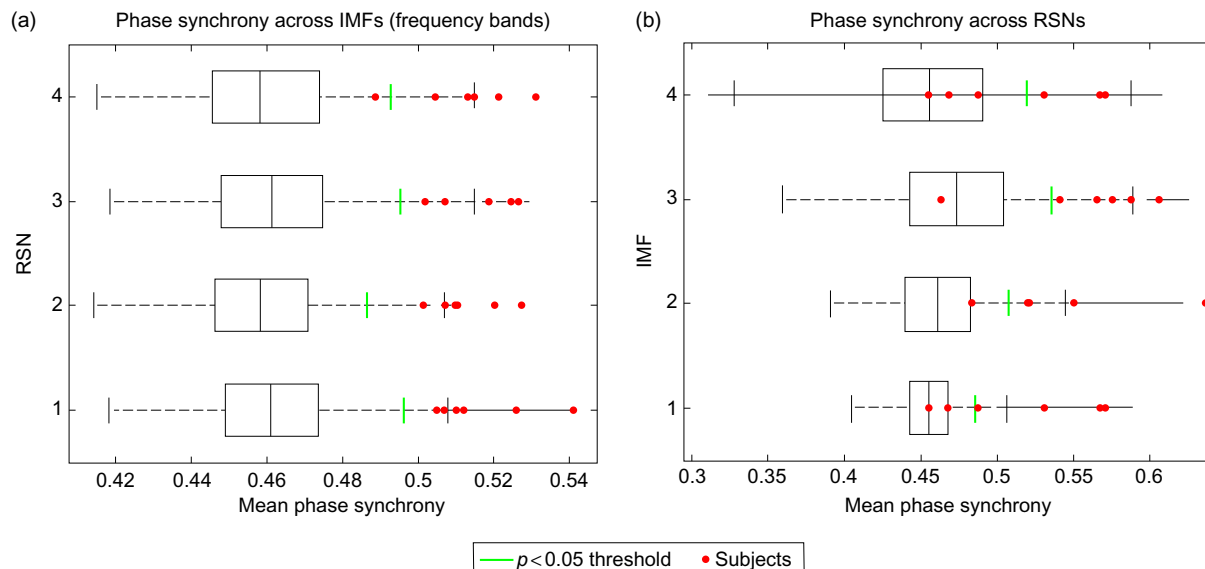
Fig. 4. Box plots of the null distributions and significance of (a) phase synchrony across IMFs within any given RSN and (b) phase synchrony across different RSNs in a given frequency band (IMF). Each box plot represents the null distributions for the mean phase synchrony. For clarity, outlier markers have been replaced by a solid line to indicate the extent of the data. The threshold for rejecting the null hypothesis at $p < 0.05$ is indicated by the green line on each distribution. The actual synchrony measurements from the six subjects are plotted using red dots.

"$1/f$" (Fox and Raichle, 2007; the power is proportional to the inverse of the frequency) and others as containing peaks generally between 0.01 and 0.04 Hz (Beckmann et al., 2005). However, this characterization is based on power spectra derived from BOLD time series, as opposed to time series more directly related to the underlying neural processes. Hemodynamic responses to neural processes are blurred and delayed, when compared with those neural processes, and the blurring downweights higher frequencies. Hence spectral analysis of BOLD data is in effect biased against estimating power at higher frequencies. We have carried out a very simple experiment to investigate the effect that deconvolving the hemodynamic blurring has on the apparent power spectra of RSNs, in order to better visualize the power spectra of the underlying neural processes.

FMRI data were obtained on a 3-T Siemens Trio with low-TR, in order to be able to separate and identify different physiological processes in the data. We acquired standard EPI resting data at $3 \times 3 \times 3$ mm, TR = 0.35 s, nine slices, 11 min. We also obtained visual activation data (with the same parameters) in order to characterize the HRF, using a repeated paradigm of 1-s flashing checkerboard followed by 15 s rest.

Analysis was carried out using FSL. The data was high-pass filtered to remove drift using a 200-s FWHM Gaussian filter and spatially smoothed with a 3-mm FWHM Gaussian kernel. ICA was applied (via the MELODIC tool Beckmann and Smith, 2004) to identify RSN spatial maps and time-courses. Using both a standard HRF (hemodynamic response function) kernel estimate (a single Gamma variate, as used in the FEAT tool in FSL), and also, separately, an
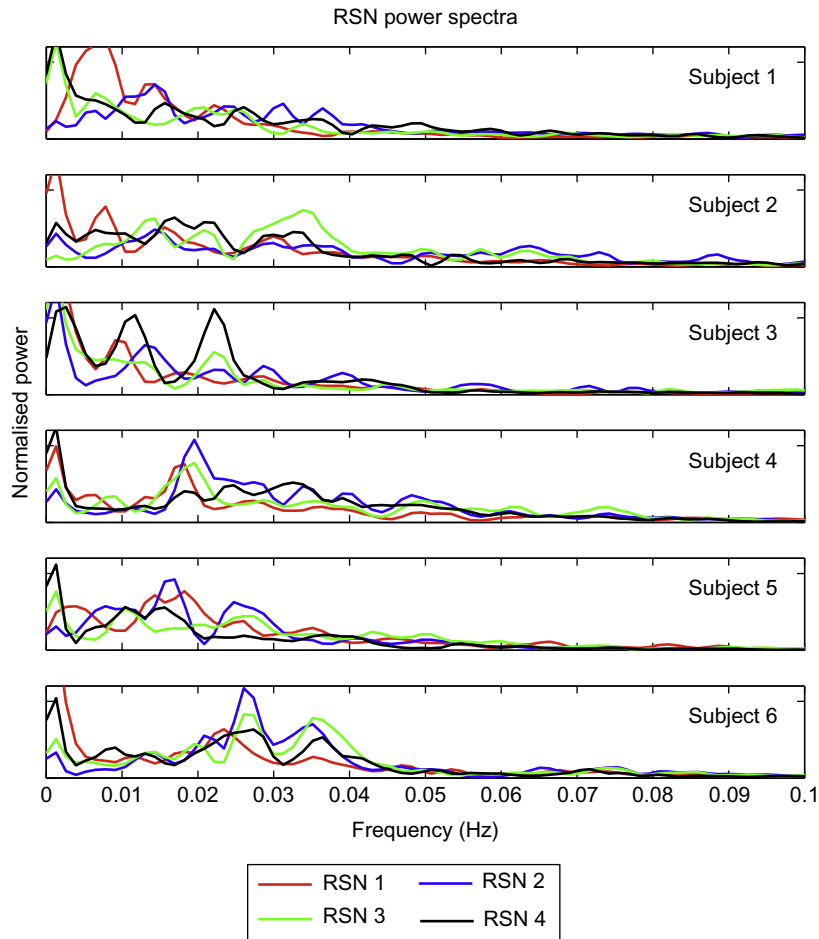
RSN power spectra

Fig. 5. All subjects' RSN power spectra, color-coded by RSN. Each panel shows the power spectra of the four RSNs of that subject. Each RSN is plotted in a different color.

empirically derived HRF kernel (using the visual activation data), we deconvolved the HRF from the RSN time-courses.[1] We then computed the

power spectrum of each deconvolved (neural) RSN time-course.

Five RSNs were identified; see one example—the DMN—in Fig. 6. The full original power spectra are shown in Fig. 7 (top row); the *y* axis is in log units so that the slight contamination of the time series by the breathing and cardiac cycles can be seen (at around 0.25 and 1 Hz, respectively). The black line shows the mean of the five RSNs. The characteristic "1/*f*" spectral distribution (seen with the log axis as a straight line)

---

[1]Note that the HRF deconvolution is accurate enough to interpret the adjusted power spectra (as seen by the fact that our results are unchanged when slightly different analytic or empirical deconvolution kernels are used), but certainly not useful for estimating the exact hemodynamic *lag* at any given region in the brain; this latter is not trivial to deconfound from neural lags and is not important for the spectral characterizations in this work.
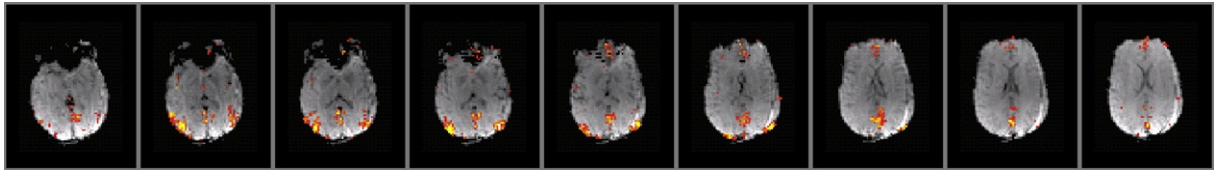
Fig. 6. Example RSN (the "default mode network") from the low-TR resting data. $3 \times 3 \times 3$ mm, TR$=350$ ms, nine slices, 11 min of subject at rest.
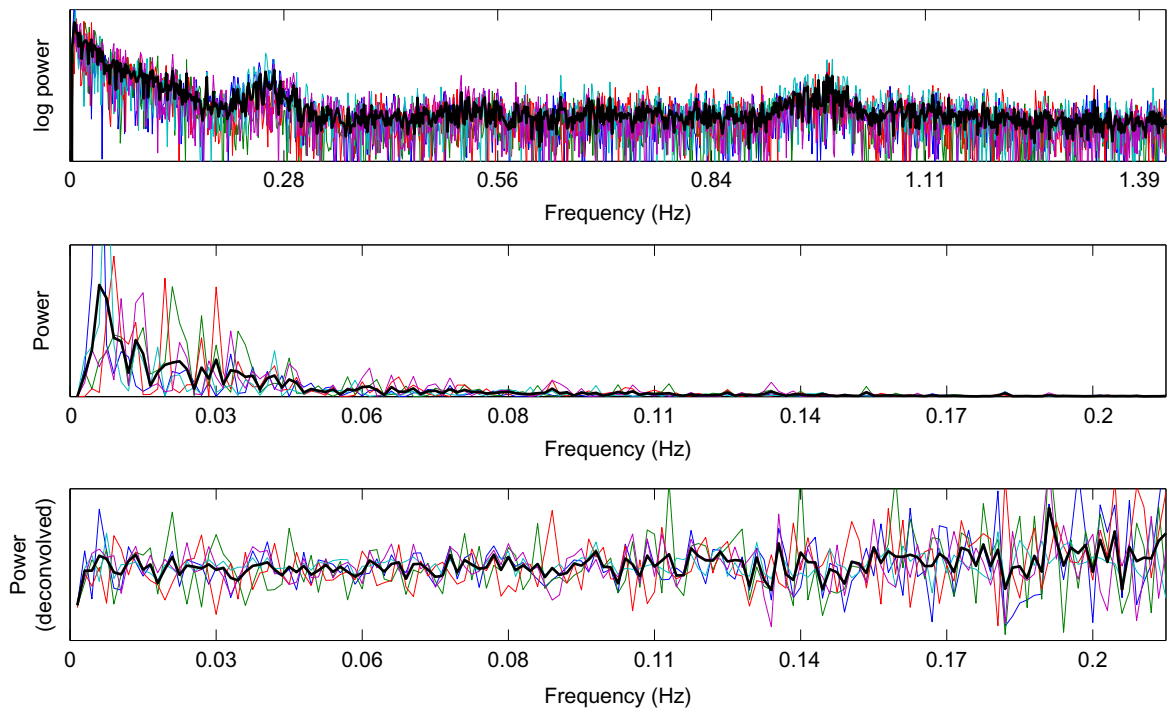

Fig. 7. Power spectra for five RSNs in low-TR (350 ms) data. The mean of all five is shown in black. *Top row*: full range of power spectra, with the *y* axis in log units, allowing visualization of the low-level contamination by breathing and cardiac artefacts. *Middle row*: BOLD power spectra for the uncontaminated frequency range of 0–0.2 Hz. *Bottom row*: "Neural" power spectra obtained by deconvolving the hemodynamic blurring from the BOLD time series.

can be seen from the lowest frequencies up to where the breathing (and thermal noise) starts to contaminate the spectra. The middle row shows the same spectra, but just concentrating on the well-estimable frequencies, up to 0.2 Hz.

The bottom row shows the same five spectra, after deconvolving the BOLD time series using the HRF and scaling all to have the same mean

level. After this deconvolution, it is clear that, up until the point of the noise contamination, the underlying neural processes appear to have a very flat power spectrum in all five RSNs seen. Very similar results are found whether using the fixed canonical Gamma-based HRF, or the data-derived HRF. The clear conclusion must be that in the frequency range estimable from this data,

namely around 0.01–0.2 Hz, the amplitude of the fluctuations in the resting neural processes appears to be constant and not in fact greater at lower frequencies.

In order to confirm that these results were not just specific to the initial subject studied, we have also applied equivalent analyses to data from a further 10 subjects using similar acquisition parameters. HRF deconvolution using the methods described above gave exactly the same qualitative results, that is, show that the "neural" spectrum is flat up to at least 0.2 Hz. Note that the time-courses used in these tests were derived from regressing the ICA spatial maps back into the original data, and so will not be biased spectrally by any dimensionality reduction in the initial ICA.

In the final section, we further explore the spectral characteristics of RSNs using data from perfusion MRI at extremely low frequencies.

RSN spectra from perfusion FMRI

It is not generally possible to investigate very low-frequency processes with BOLD FMRI data, because of various sources of drift that cannot easily be separated from real signal of interest. Hence the spectral behavior of RSNs below approximately 0.01 Hz has not been well characterized previously. However, perfusion FMRI, using ASL (arterial spin labeling), is not sensitive to drifts to the same extent, and so we used this in order to investigate frequencies as low as 0.001 Hz. ASL is primarily sensitive to blood *flow* (unlike BOLD FMRI, which is sensitive to both blood flow and *oxygenation*) and can respond to many physiological processes, some related and others unrelated to neuronal fluctuations. However, several independent components derived from perfusion data clearly show the same spatial patterns as RSNs reported in the literature, and now widely accepted as being neuronal in origin. Hence, it is reasonable to interpret these components in the ASL data as informative about the characteristics of the spontaneous neuronal fluctuations in RSNs.

We acquired whole-brain ASL data from 19 subjects, as well as structural images that were used to aid coregistration to standard (MNI152) space. The data were obtained using a Siemens 3T Trio with a single-channel radio-frequency transmit/receive head coil: 20 axial slices, $4 \times 4 \times 6$ mm voxels, 1.2 mm slice gap. Signals within the inferior and the superior halves of the brain (each with 10 axial slices) were acquired separately, in an alternating manner. For "tag" acquisitions, 1.6 s of continuous tagging was used, followed by a postlabeling delay of 0.5 s and the acquisition of the lower slice stack. A further 1.6 s of tagging was then applied followed by a postlabeling delay of 1 s before the acquisition of the upper slice stack. The different postlabeling delays account for differences in arterial arrival time between the two slice stacks. "Control" labels used a cosine-modulated, magnetic transfer contrast (MTC)-matched pulse train (Alsop and Detre, 1998). The labeling offset was located 10 cm inferior to the center of the 20 slices. Acquisition was in ascending order and required approximately 6 s for a whole-brain volume.

Data was corrected for head motion using MCFLIRT (Jenkinson et al., 2002), spatially smoothed by 5 mm FWHM, and then tag-control subtracted using sinc-based shifting of both tag and control time series to the temporal-mid-point followed by subtraction. All 4D preprocessed data was registered into standard space, and a single groupwise ICA was run using MELODIC (Beckmann and Smith, 2004) in "temporal concatenation mode"—effectively concatenating all subjects' datasets temporally before PCA-based dimensionality reduction to 40 components, followed by ICA unmixing to identify the 40 primary effects present in the multisubject dataset. At least six components were found that clearly matched RSNs commonly seen in resting BOLD data, including the DMN (see Fig. 8) and auditory, visual, cognitive, and fronto-parietal networks. The 40 groupwise spatial maps were
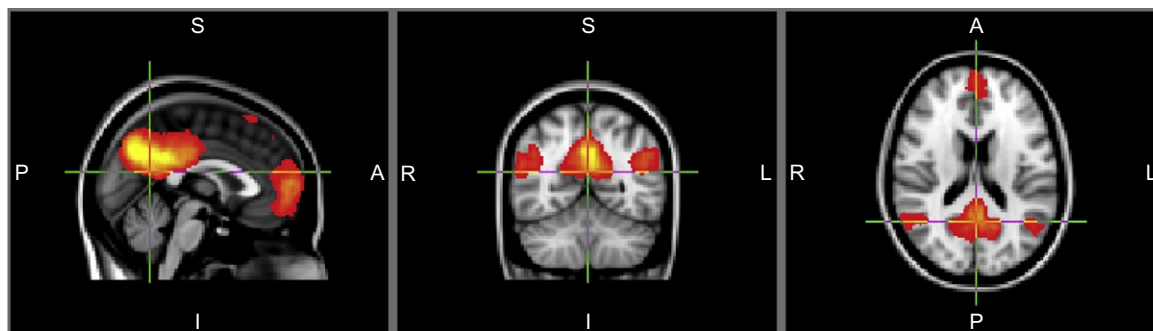
Fig. 8. Example RSN (the "default mode network") from the perfusion (ASL) data.

regressed (as spatial regressors in a multiple regression) into each subject's dataset separately, in order to generate subject-specific versions of the 40 components' time-courses (Filippini et al., 2009). Time-courses from the six components clearly identified as RSNs were then studied for their spectral characteristics.

The results are shown in Fig. 9; each panel shows spectra for a different RSN, with each color showing the spectrum from a different subject. The spectra gradually fall to zero above 0.03 Hz, primarily because of perfusion–subtraction preprocessing (in addition to the effect of the hemodynamic smoothing).[2] However, below this, down to the lowest frequency estimable from these session durations (i.e., ∼0.001 Hz), the spectra are remarkably flat, not showing any noticeable raising of resting fluctuation amplitude at lower frequencies.

Discussion

RSNs have long been described as "low-frequency fluctuations" in the BOLD signal. However, even though some attempts have been made to shed some light on their temporal characteristics (Cordes et al., 2001; Fukunaga et al., 2006), there still remain questions regarding the exact contributing frequencies, if more than one, and regarding the relationship between these frequencies, and indeed between the different RSNs. Given the common assumption that RSN processes are simple, slow oscillations in BOLD, the goal of this work was to try isolating different underlying oscillatory processes, if any, and determine the relationship between them within and across subjects. We used EMD as a tool to find the underlying oscillations associated with a set of RSNs. In contrast to traditional Fourier analysis, EMD was chosen as it is capable of decomposing a signal into its intrinsic modes of oscillation without any assumption of linearity, stationarity, or imposing *a priori* assumptions on the frequencies of interest. This analysis also provides a way to examine the phase characteristics of the different RSNs.

Looking at the EMD, ICA and power spectra results, some new findings have been made, which enhance our understanding of these still mysterious phenomena. The main finding of the EMD/ICA analysis is that RSNs are *not* simply low-frequency fluctuations in the BOLD signal. This was evident in that RSNs were obtained using GLM analysis with the IMFs as regressors. Each IMF occupies a specific frequency band, and thus the RSNs have been shown to be correlated with

---

[2]We only show raw spectra and not HRF-deconvolved; the frequencies present in the tag-control subtracted time series are sufficiently low that HRF deconvolution made almost no difference to these plots.
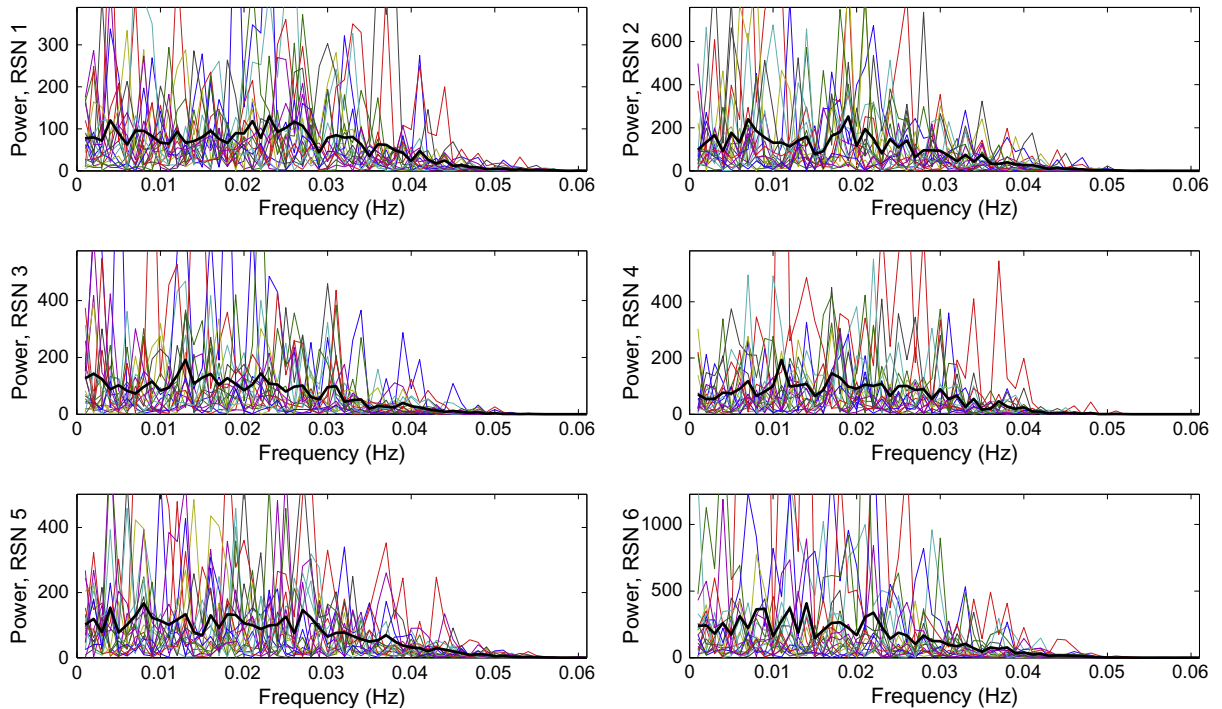
Fig. 9. Power spectra for six RSNs in the perfusion data with a different RSN shown in each panel. The different colors are for the 19 different subjects, with the mean power spectrum shown in black. From approximately 0.03 down to 0.001 Hz, the power spectra are strikingly constant.

signals of different frequencies and not just a specific slow frequency. Further, this finding was validated using a totally independent method: filtering the data using a bank of filters, then applying ICA. Again, the RSNs appeared in all the filtered data and not as a single narrow-band oscillatory process. The DSC was used to quantify how spatially similar the reproduced RSNs were compared to the original. The values obtained using DSC were very high for different RSNs and subjects. Surprisingly, the frequency band that produced the most similar RSNs to the original was FB2 (0.02–0.05 Hz), and not FB3, where the commonly reported ∼0.015 Hz peak frequency lies.

At this point, it is worth clarifying the GLM approach was not circular in nature. The main reason is that the time-courses obtained by ICA are not guaranteed to include signals exclusive to the ICA map, for example, a global signal common to these (and other areas) will also be represented in the time-course, even though it is not exclusive to the network. Hence, decomposing an RSN time-course signal and using the IMFs in the GLM was not guaranteed to reproduce the RSN at all frequencies, and indeed that does not occur in all frequencies, that is, IMFs above 4 did not reproduce the RSN. This same reasoning also applies using the filter-bank approach used to verify our results.

Performing EMD on the time-courses of the RSNs gave us the opportunity to further investigate the relationship between the RSNs and between the different oscillatory frequencies within an RSN. Phase synchrony in a specific frequency band across the different RSNs may

indicate global regulation at that frequency. The results indicated that, for most of the subjects, there is a significant phase synchrony at the frequency bands of IMFs 2 and 3 between the RSNs (Fig. 4b). This is not very surprising in that we know that these frequency bands are the ones traditionally linked with RSNs. But as mentioned previously, the frequency band with the highest synchrony level across RSNs (IMF3) was not the same frequency band that reproduced the highest similarity compared to the original RSN. This may be due to the fact that at this frequency we are looking at a more global network with higher synchrony-more power, but less specific. In our case, the evidence for large networks is the phase synchrony across all the RSNs. However, there is also evidence for local regulation/activation in that at higher frequencies we have RSNs but with less phase synchrony between them, while still spatially scoring higher when using Dice spatial similarity.

Taking each RSN individually, the results were statistically much more significant (Fig. 4a). The mean phase synchrony between the different IMFs (different frequency bands) of any given RSN was significant in almost all subjects. This indicates that the underlying process of each RSN is a complex process with interdependence between the different frequencies, that is, the different frequencies are not completely independent processes that happen to be active in the same RSN.

In two additional independent studies of specific aspects of RSN power spectra, we were able to demonstrate that estimating the underlying neuronal processes using deconvolution also suggests a broadband neuronal process, with no evidence of the classic "$1/f$" behavior. This was also evident from the perfusion data where we were able to look at extremely low frequencies. We see a flat frequency response across the full range estimable across our experiments: from 0.001 to 0.2 Hz. While the difference between the deconvolved spectra and spectra commonly reported in the BOLD RSN literature are clearly explicable as simply being due to our application of the deconvolution, these results are still in contradiction to electrophysiological experiments that support the "$1/f$" description of RSN temporal behavior. It is possible that this difference could be explained by the different ways in which the RSN processes are identified within the different modalities: in the case of resting FMRI data, well-established analyses (such as ICA) are widely considered to do a good job of identifying "RSNs" (and separating them from other components in the data), and their spatial characteristics are, in general, readily identifiable; however, in the case of electrophysiological data, it has not yet been established exactly which components (frequency bands, etc.) correspond to the RSNs seen in FMRI data, and thus previous spectral characterizations are quite likely mixing different physiological processes in with "RSNs," confounding clear spectral interpretations.

It would be premature to attempt to draw specific new interpretations regarding the biological processes underlying RSNs, from the new information regarding their spectral characteristics presented in this work. What these results do provide, however, are new insights about how RSNs should be viewed and analyzed. It is clear that simply characterizing RSNs by their peak frequencies loses the full richness of the RSN processes. RSNs should be treated as complex processes that exhibit long and short temporal correlation and as processes with intricate relations between them. Characteristics such as the phase synchrony across different RSNs and across different frequencies should be considered when comparing RSNs between disease and control groups. For example, it might be the case that for some neurodegenerative diseases, the synchrony across the RSNs or the autocorrelation structure of their time-courses changes. At this stage, these are merely speculations. What is not, though, is the fact that RSNs exhibit complex temporal characteristics and should be treated as such when analyzed.

Acknowledgments

References

Alsop, D. C., & Detre, J. A. (1998). Multisection cerebral blood flow MR imaging with continuous arterial spin labeling. *Radiology*, *208*, 410–416.

Beckmann, C., De Luca, M., Devlin, J., & Smith, S. (2005). Investigations into resting-state connectivity using independent component analysis. *Philosophical Transactions of the Royal Society*, *360*(1457), 1001–1013.

Beckmann, C., & Smith, S. (2004). Probabilistic independent component analysis for functional magnetic resonance imaging. *IEEE Transactions on Medical Imaging*, *23*(2), 137–152.

Bell, A., & Sejnowski, T. (1995). An information-maximisation approach to blind separation and blind deconvolution. *Neural Computation*, *7*(6), 1129–1159.

Biswal, B., Yetkin, F., Haughton, V. M., & Hyde, J. (1995). Functional connectivity in the motor cortex of resting human brain using echo-planar MRI. *Magnetic Resonance in Medicine*, *34*, 537–541.

Chang, C., & Glover, G. (2010). Time-frequency dynamics of resting-state brain connectivity measured with fMRI. *NeuroImage*, *50*, 81–98.

Comon, P. (1994). Independent component analysis—A new concept? *Signal Processing*, *36*, 287–314.

Cordes, D., Haughton, V. M., Arfanakis, K., Carew, J. D., Turski, P. A., Moritz, C. H., et al. (2001). Frequencies contributing to functional connectivity in the cerebral cortex in "resting-state" data. *AJNR. American Journal of Neuroradiology*, *22*(7), 1326–1333.

Damoiseaux, J., Beckmann, C., Sanz Arigita, E., Barkhof, F., Scheltens, P., Stam, C., et al. (2008). Reduced resting-state brain connectivity in the 'default network' in normal aging. *Cerebral Cortex*, *18*(8), 1856–1864.

Damoiseaux, J., Rombouts, S., Barkhof, F., Scheltens, P., Stam, C., Smith, S., et al. (2006). Consistent resting-state networks across healthy subjects. *Proceedings of the National Academy of Science of the United States of America*, *103*(37), 13848–13853.

De Luca, M., Beckmann, C., Behrens, T., Clare, S., Matthews, P., De Stefano, N., et al. (2002). Low frequency signals in FMRI—"Resting state networks" and the "intensity normalisation problem". In *Proceedings of the International Society of Magnetic Resonance in Medicine*.

De Luca, M., Beckmann, C. F., De Stefano, N., Matthews, P. M., & Smith, S. M. (2006). fMRI resting state networks define distinct modes of long-distance interactions in the human brain. *NeuroImage*, *29*(4), 1359–1367.

Delorme, A., & Makeig, S. (2004). EEGLAB: An open source toolbox for analysis of single-trial EEG dynamics including independent component analysis. *Journal of Neuroscience Methods*, *134*(1), 9–21.

Filippini, N., MacIntosh, B., Hough, M., Goodwin, G., Frisoni, G., Smith, S., et al. (2009). Distinct patterns of brain activity in young carriers of the APOE-e4 allele. *Proceedings of the National Academy of Science of the United States of America*, *106*, 7209–7214.

Fox, M. D., & Raichle, M. E. (2007). Spontaneous fluctuations in brain activity observed with functional magnetic resonance imaging. *Nature Reviews. Neuroscience*, *8*(9), 700–711.

Fukunaga, M., Horovitz, S. G., van Gelderen, P., de Zwart, J. A., Jansma, J. M., Ikonomidou, V. N., et al. (2006). Large-amplitude, spatially correlated fluctuations in BOLD fMRI signals during extended rest and early sleep stages. *Magnetic Resonance Imaging*, *24*(8), 979–992.

Greicius, M. D., Srivastava, G., Reiss, A. L., & Menon, V. (2004). Default-mode network activity distinguishes Alzheimer's disease from healthy aging: Evidence from functional MRI. *Proceedings of the National Academy of Sciences of the United States of America*, *101*(13), 4637–4642.

Huang, N. E., & Shen, S. S. P. (Eds.), (2005). *Hilbert-Huang transform and its applications. Volume 5 of interdisciplinary mathematical sciences*. Hackensack, NJ: World Scientific Publishing Co. Pvt. Ltd, Including papers from the Hilbert-Huang Transform (HHT) mini-symposium at the joint meeting between the Society for Industrial and Applied Mathematics and the Canadian Applied and Industrial Mathematics Society held in Montreal, QC, June 2003.

Huang, N. E., Shen, Z., & Long, S. R. (1999). A new view of nonlinear water waves: The Hilbert spectrum. In *Annual review of fluid mechanics, Vol. 31* (pp. 417–457). Palo Alto, CA: Annual Reviews.

Huang, N. E., Shen, Z., Long, S. R., Wu, M. C., Shih, H. H., Zheng, Q., et al. (1998). The empirical mode decomposition and the Hilbert spectrum for nonlinear and non-stationary time series analysis. *Royal Society of London. Proceedings. Series A. Mathematical, Physical and Engineering Sciences*, *454*(1971), 903–995.

Huang, N. E., Wu, M.-L. C., Long, S. R., Shen, S. S., Qu, W., Gloersen, P., et al. (2003). A confidence limit for the empirical mode decomposition and Hilbert spectral analysis. *Royal Society of London. Proceedings. Series A. Mathematical, Physical and Engineering Sciences*, *459*(2037), 2317–2345.

Jenkinson, M., Bannister, P., Brady, J., & Smith, S. (2002). Improved optimisation for the robust and accurate linear registration and motion correction of brain images. *NeuroImage*, *17*(2), 825–841.

Lai, S., Qiu, M., Niazy, R. K., & Panzer, V. (2002). Effects of normal aging on the brain functional connectivity of primary motor cortex: Preliminary FMRI results. In: *Proceedings of the 8th International Conference on Functional Mapping of the Human Brain* Sendai, Japan.

Lowe, M. J., Mock, B. J., & Sorenson, J. A. (1998). Functional connectivity in single and multislice echoplanar imaging using resting-state fluctuations. *NeuroImage*, *7*(2), 119–132 Clinical Trial.

Mason, M. F., Norton, M. I., Van Horn, J. D., Wegner, D. M., Grafton, S. T., & Macrae, C. N. (2007). Wandering minds: The default network and stimulus-independent thought. *Science*, *315*(5810), 393–395.

McKeown, M. J., Makeig, S., Brown, G. G., Jung, T. P., Kindermann, S. S., Bell, A. J., et al. (1998). Analysis of fMRI data by blind separation into independent spatial components. *Human Brain Mapping*, *6*(3), 160–188.

Niazy, R. K., Qiu, M., Deng, Z., Enderle, J., & Lai, S. L. (2002). Normal aging and brain functional connectivity of primary motor cortex: A functional MRI (fMRI) study. *Proceedings of the IEEE 28th Annual Northeast Bioengineering Conference* Philadelphia, PA.

Raichle, M. E., MacLeod, A. M., Snyder, A. Z., Powers, W. J., Gusnard, D. A., & Shulman, G. L. (2001). A default mode of brain function. *Proceedings of the National Academy of Sciences of the United States of America*, *98*(2), 676–682.

Rilling, G., Flandrin, P., & Gonçalvès, P. (2003). On empirical mode decomposition and its algorithms. *IEEE-EURASIP workshop on nonlinear signal and image processing NSIP-03* Grado, Italy.

Rombouts, S., Damoiseaux, J., Goekoop, R., Barkhof, F., Scheltens, P., Smith, S., et al. (2009). Model-free group analysis shows altered bold fMRI networks in dementia. *Human Brain Mapping*, *30*(1), 256–266.

Smith, S., Fox, P., Miller, K., Glahn, D., Fox, P., Mackay, C., et al. (2009). Correspondence of the brain's functional architecture during activation and rest. *Proceedings of the National Academy of Sciences of the United States of America*, *106*(31), 13040–13045.

Xiong, J., Parsons, L. M., Gao, J. H., & Fox, P. T. (1999). Interregional connectivity to primary motor cortex revealed using MRI resting state images. *Human Brain Mapping*, *8*(2–3), 151–156.